

Satellite-Free Training for Drone-View Geo-Localization

Tao Liu

liutao23@njust.edu.cn

Nanjing University of Science and Technology
Nanjing, Jiangsu, China

Kan Ren

Nanjing University of Science and Technology
Nanjing, Jiangsu, China
k.ren@njust.edu.cn

Yingzhi Zhang

University of Tsukuba

Tsukuba, Ibaraki, Japan

zhang_y@css.risk.tsukuba.ac.jp

Xiaoqi Zhao

Yale University

New Haven, Connecticut, USA

xiaoqi.zhao@yale.edu

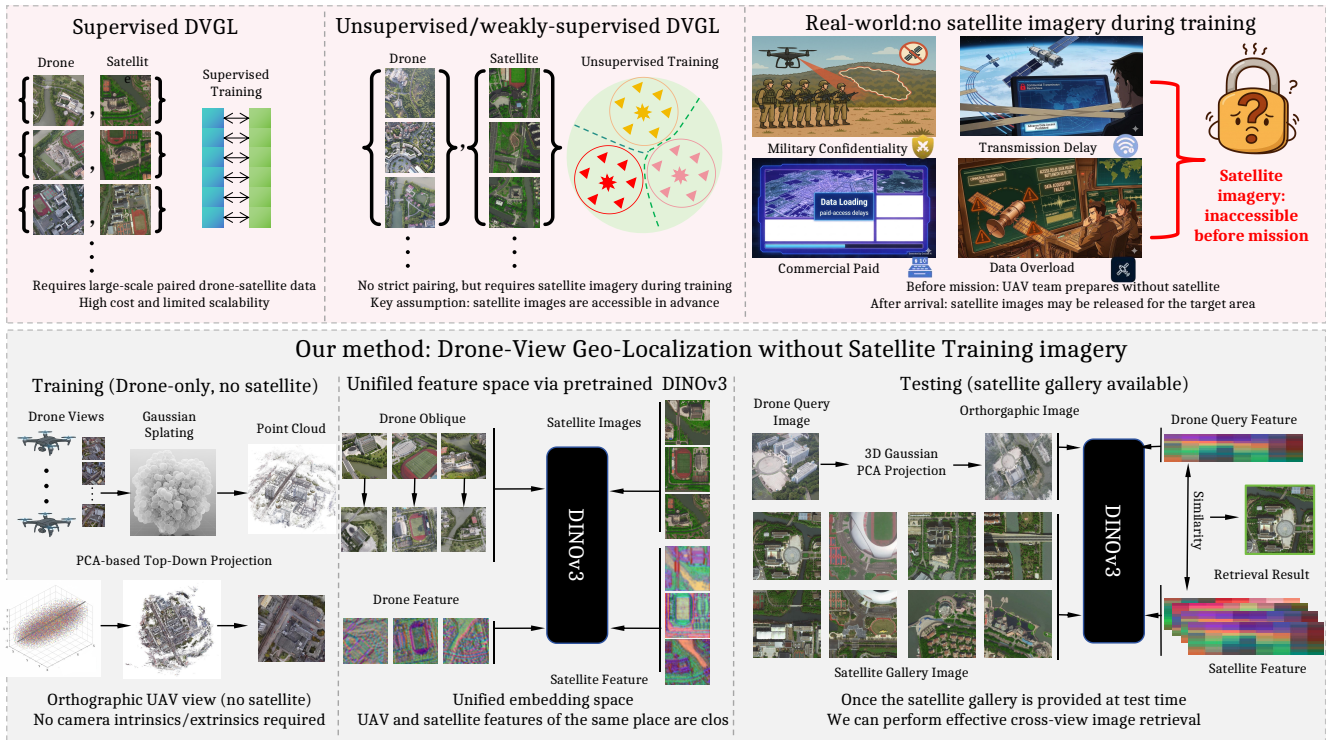


Figure 1: Motivation and overview of the proposed satellite-free training (SFT) framework. Unlike existing DVGL methods that rely on satellite imagery during training, our method uses only multi-view drone images. The UAV sequence is reconstructed into a 3D scene and converted into a pseudo-orthophoto, which is then encoded by a frozen DINOv3 backbone. The retrieval space is constructed solely from drone-side features via drone-only GMM learning and Fisher vector aggregation, so satellite tiles are encoded at test time in a space induced entirely by drone data.

Abstract

Drone-view geo-localization (DVGL) aims to determine the location of drones in GPS-denied environments by retrieving the corresponding geotagged satellite tile from a reference gallery given UAV observations of a location. In many existing formulations, these observations are represented by a single oblique UAV image. In contrast, our satellite-free setting is designed for multi-view UAV sequences, which are used to construct a geometry-normalized

UAV-side location representation before cross-view retrieval. Existing approaches rely on satellite imagery during training, either through paired supervision or unsupervised alignment, which limits practical deployment when satellite data are unavailable or restricted. In this paper, we propose a satellite-free training (SFT) framework that converts drone imagery into cross-view compatible representations through three main stages: drone-side 3D scene reconstruction, geometry-based pseudo-orthophoto generation, and satellite-free feature aggregation for retrieval. Specifically, we first reconstruct dense 3D scenes from multi-view drone images using 3D Gaussian splatting and project the reconstructed geometry into

pseudo-orthophotos via PCA-guided orthographic projection. This rendering stage operates directly on reconstructed scene geometry without requiring camera parameters at rendering time. Next, we refine these orthophotos with lightweight geometry-guided inpainting to obtain texture-complete drone-side views. Finally, we extract DINOv3 patch features from the generated orthophotos, learn a Fisher vector aggregation model solely from drone data, and reuse it at test time to encode satellite tiles for cross-view retrieval. Experimental results on University-1652 and SUES-200 show that our SFT framework substantially outperforms satellite-free generalization baselines and narrows the gap to methods trained with satellite imagery.

CCS Concepts

• **Computing methodologies** → **Visual content-based indexing and retrieval.**

Keywords

Drone-view geo-localization, Gaussian splatting, foundation models

ACM Reference Format:

Tao Liu, Yingzhi Zhang, Kan Ren, and Xiaoqi Zhao. 2026. Satellite-Free Training for Drone-View Geo-Localization. In . ACM, New York, NY, USA, 14 pages. <https://doi.org/10.1145/nnnnnnnn.nnnnnnnn>

1 Introduction

Drone-view geo-localization (DVGL) aims to determine the location of drones in GPS-denied environments by retrieving the corresponding geotagged satellite tile from a reference gallery for a given drone image [38]. This task is crucial for navigation and situational awareness in scenarios where GPS signals are unavailable or unreliable.

The upper part of Fig. 1 shows the common DVGL training setups and the discrepancy between these assumptions and real-world practice. Previous supervised [3, 29, 31, 32, 35, 45] and unsupervised [1, 2, 14, 16, 18] methods assume that satellite imagery is accessible during training, either for paired annotations or iterative optimization. In reality, satellite data may be unavailable in advance due to factors such as military confidentiality, commercial transmission restrictions, data volume bottlenecks, and paid-access delays, and only become accessible after drone teams have already arrived on site [11, 25, 40]. This raises a central challenge: *can DVGL be trained only on drone images yet still retrieve satellite tiles accurately at test time?*

Inspired by recent advances in neural scene representations such as Neural Radiance Fields (NeRF) [23] and 3D Gaussian Splatting (3DGS) [15], which enable multi-view consistent reconstruction and high-quality view synthesis, we propose a satellite-free training (SFT) framework designed for DVGL in the absence of satellite supervision. In this paper, “satellite-free” refers to the downstream DVGL training pipeline: no satellite images are used for task-specific training, adaptation, vocabulary construction, or retrieval-space learning. We use a frozen public web-pretrained DINOv3 backbone as a generic feature extractor, rather than any satellite-specialized model.

Our central idea is to convert raw multi-view drone footage into an overhead proxy representation that approximates the appearance and geometry of satellite nadir imagery. We first reconstruct each scene using 3DGS to obtain a high-fidelity Gaussian field that captures both structural geometry and view-dependent appearance. To convert this reconstructed scene into an explicit overhead view, we perform importance-guided sampling on Gaussians to extract a dense point cloud, followed by PCA-based ground-plane alignment and orthographic projection. Importantly, this pseudo-orthophoto generation stage operates on reconstructed scene geometry rather than relying on camera parameters during rendering. A “soft-roof” compositing strategy is adopted to gently fuse multi-depth structures, suppress perspective distortion, and preserve building contours. The orthographic renderings are then refined through lightweight geometry-guided corrections and LaMa-based completion [33], yielding texture-consistent pseudo-orthophotos that serve as UAV-side location representations. For representation learning, we employ DINOv3 [30] to extract semantically rich patch-level descriptors from the pseudo-orthophotos. A Gaussian mixture model (GMM) is learned exclusively from these drone-generated patches to build a modality-agnostic visual vocabulary, upon which Fisher vectors [28] are computed to aggregate patches into compact global descriptors. This choice provides two benefits: FV aggregation complements DINOv3’s global invariances with fine-grained texture cues, and the drone-trained GMM introduces a structural prior that transfers surprisingly well to unseen satellite images. At test time, satellite tiles are processed using the same DINOv3 and Fisher vector pipeline, producing descriptors that reside in the same embedding space as the drone pseudo-orthophotos. Retrieval is performed directly in this shared space, enabling cross-view matching without any form of satellite supervision, paired data, or satellite-side adaptation during training.

In summary, our main contributions are as follows:

- We introduce a satellite-free training (SFT) framework that enables drone-view geo-localization using only drone imagery during training.
- We develop a unified drone-satellite retrieval pipeline that integrates 3DGS reconstruction, pseudo-orthophoto generation, DINOv3 feature extraction, and Fisher vector aggregation to convert multi-view drone images into cross-view compatible representations.
- We adapt the pipeline for geo-localization by introducing geometry-based orthographic rendering after reconstruction, geometry-guided inpainting, and GMM-based Fisher vector aggregation to construct a unified embedding space tailored for cross-view retrieval.
- Extensive experiments on University-1652 and SUES-200 demonstrate that our SFT framework substantially outperforms reproduced generalization baselines and narrows the gap to methods trained with satellite imagery.

2 Related Work

2.1 Drone-View Geo-Localization

Drone-view geo-localization (DVGL) is a cross-view retrieval task that aims to match oblique drone images with nadir satellite or aerial imagery. Early supervised methods [3, 5, 19, 29, 31, 32, 35,

45] typically rely on large-scale paired drone-satellite annotations and optimize cross-view similarity using metric learning. These methods often incorporate local pattern decoupling, multi-region aggregation, or diffusion-based generation to improve robustness and fine-grained discrimination.

To reduce the need for strict pairing, recent works explore unsupervised or self-supervised paradigms. AnyLoc [14] directly employs pre-trained DINOv2 features [26] with unsupervised aggregation for place recognition, but it still faces a significant cross-view gap. EM-CVGL [18], CDIKTNet [1], DMNIL [2], and other recent methods [16, 36] adapt foundation models using pseudo-labels, contrastive objectives, or domain adaptation in the presence of satellite images. Li et al. [17] further incorporate 3DGS to render satellite-like views from multi-view drone images. Unlike these approaches, which require satellite data during training, we focus on building a cross-view embedding space using only drone images that generalizes to satellite tiles at test time.

2.2 Multi-View Reconstruction and 3DGS

Classical visual localization pipelines reconstruct sparse or dense point clouds (e.g., COLMAP [27]) and perform image-to-structure matching [12, 41]. NeRF-based methods [23, 24, 44] represent scenes as continuous radiance fields and enable photorealistic novel-view synthesis, but they are often too slow for large-scale DVGL. 3DGS [15] provides an explicit, real-time alternative by modeling scenes as sets of Gaussian primitives and rendering them via rasterization. Recent works adopt 3DGS for map representation, localization, and pose estimation [13, 22]. In contrast, our pipeline leverages 3DGS to normalize drone viewpoints and generate pseudo-orthophotos, rather than constructing a global Gaussian map of the environment.

3 Proposed Method

3.1 Satellite-Free Problem Setting and Overview

We consider a DVGL setting where only multi-view drone imagery is available during training. Let $\mathcal{D}_{\text{train}}^{\text{UAV}}$ denote drone image sequences captured at multiple locations, each containing overlapping oblique views of the same scene. Satellite images and their geo-tags, denoted as \mathcal{G}^{Sat} , are unavailable during training and are revealed only at test time.

Our goal is to learn, using only $\mathcal{D}_{\text{train}}^{\text{UAV}}$, a representation and retrieval pipeline that can match UAV-side location representations with satellite tiles without any additional fine-tuning. At inference time, the available multi-view UAV observations of a location are reconstructed into a pseudo-orthophoto, which serves as the drone-side representation—used as the query in Drone→Satellite retrieval and as the gallery item in Satellite→Drone retrieval.

As shown at the bottom of Fig. 1, our method has two components: (1) **drone-side 3D reconstruction and pseudo-orthophoto generation**, based on 3DGS point-cloud sampling, PCA-based orthographic projection, and geometry-guided inpainting; and (2) a **satellite-free cross-view representation**, built on a frozen DINOv3 backbone and Fisher vectors, where the GMM vocabulary is learned only from drone pseudo-orthophotos and reused to encode satellite tiles at test time.

Notably, the frozen DINOv3 backbone does not itself define a drone-specific embedding space. Instead, it acts as a shared patch

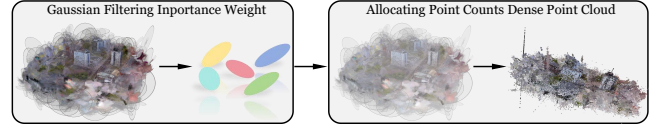


Figure 2: Illustration of converting a 3D Gaussian field into a dense point cloud.

feature extractor, while the final retrieval space is induced by the GMM vocabulary and Fisher statistics learned exclusively from drone-side pseudo-orthophotos.

3.2 Drone-Side Pseudo-Orthophoto Generation

3.2.1 3DGS Reconstruction and Point-Cloud Conversion. Given a multi-view drone image sequence $\{I_m\}_{m=1}^M$, we first run COLMAP [27] to obtain camera poses $\{T_m\}$ and an initial dense point cloud. We then optimize a 3DGS (3DGS) scene [15] with the official implementation, yielding a set of Gaussians:

$$G = \{g_i\}_{i=1}^{N_g}. \quad (1)$$

Each Gaussian is parameterized as

$$g_i = (\boldsymbol{\mu}_i, \boldsymbol{\Sigma}_i, \alpha_i, \mathbf{c}_i), \quad (2)$$

where $\boldsymbol{\mu}_i$, $\boldsymbol{\Sigma}_i$, α_i , and \mathbf{c}_i denote its center, covariance, opacity, and spherical-harmonic color coefficients, respectively.

To avoid expensive orthographic rendering of anisotropic Gaussians, we convert G into a dense colored point cloud \mathcal{P} via importance-weighted sampling (Fig. 2). For each g_i , a visibility vector \mathbf{v}_i is accumulated over views, and an importance score is defined as

$$\tilde{w}_i = \alpha_i \|\mathbf{v}_i\|_1. \quad (3)$$

This score is then normalized to w_i^{imp} and used to allocate samples. Points are drawn inside each Gaussian under the Mahalanobis-distance constraint:

$$d_M(\mathbf{x}) = \sqrt{(\mathbf{x} - \boldsymbol{\mu}_i)^\top \boldsymbol{\Sigma}_i^{-1} (\mathbf{x} - \boldsymbol{\mu}_i)} \leq \tau_M, \quad (4)$$

where τ_M is a fixed Mahalanobis-distance radius. Each sampled position \mathbf{p}_j inherits its color \mathbf{c}_j and normal \mathbf{n}_j from the corresponding source Gaussian. This results in the final point cloud:

$$\mathcal{P} = \{(\mathbf{p}_j, \mathbf{c}_j, \mathbf{n}_j)\}_{j=1}^{N_p}. \quad (5)$$

See supplementary material A for details.

3.2.2 PCA-based Ground Plane and Soft-Roof Rendering. Figure 3 illustrates the pipeline from the dense point cloud \mathcal{P} to the final pseudo-orthophoto. Starting from the reconstructed 3D geometry, we estimate the ground plane via RANSAC [7], initialized by PCA, and define a local 2D orthonormal basis $\{\mathbf{u}, \mathbf{v}\}$. Each 3D point is then expressed as (u_j, v_j, h_j) , where h_j denotes the height above the plane. Based on this representation, we generate an adaptive raster that satisfies a target point density and memory budget. In this way, the orthographic rendering is performed directly on reconstructed scene geometry, without requiring camera parameters in the rendering stage.

Next, we apply a two-layer compositing scheme. Near-ground points form the *ground layer*, while points above an estimated

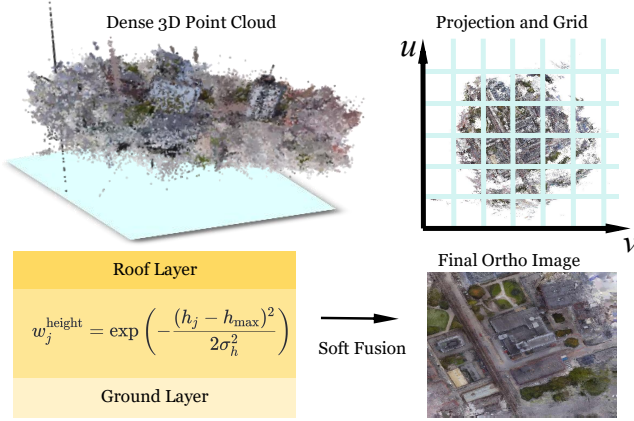


Figure 3: Pipeline of PCA-based ground plane projection and soft-roof rendering. Top left shows a dense point cloud and estimated ground plane. Top right depicts the projection onto a raster grid. Bottom left illustrates two-layer compositing with the roof layer weighted by a height-adaptive Gaussian kernel. Bottom right displays the resulting UAV pseudo-orthophoto.

roof height contribute to the *roof layer* through a height-adaptive weight:

$$w_j^{\text{height}} = \exp\left(-\frac{(h_j - h_{\text{roof}})^2}{2\sigma_h^2}\right). \quad (6)$$

Finally, the roof and ground layers are combined through soft alpha compositing driven by the roof-confidence mask, allowing elevated structures to be preserved while suppressing hard depth discontinuities. See supplementary material B for details.

3.2.3 Geometry-Guided and LaMa Inpainting. Small missing regions are first handled through morphology-based hole detection and classical inpainting. Specifically, a hole mask M_{hole} is derived from regions with low Gaussian coverage or low confidence, for example, $\alpha < \tau_\alpha$ or point support $< \tau_s$, while color cues are used only as secondary evidence. Telea inpainting is applied to tiny gaps, and KNN-based propagation on the (u, v) raster is used for compact contiguous regions.

Large missing areas, defined as connected components with area $> \tau_A$, are completed using the pre-trained LaMa network [33] with a dilated M_{hole} . To preserve structural fidelity, LaMa is restricted to background-like regions and prevented from crossing roof-ground boundaries. Seam transitions are further refined with feathering or Poisson blending.

Geometry guidance ensures that hole detection and classical filling operate in local roof or ground frames on the (u, v) raster, with anisotropic smoothing aligned to planar tangents. See supplementary material C for details.

The final image I_{final} is therefore a geometry-consistent, texture-complete drone-view pseudo-orthophoto. For downstream retrieval, we use the center crop aligned to the raster origin.

3.3 Satellite-Free DINOv3+Fisher Representation

3.3.1 Patch-Level Feature Extraction. We use a frozen DINOv3 vision transformer [30] as the feature extractor. Each image, either a drone pseudo-orthophoto or a satellite tile, is resized, center-cropped, and split into patches, while the CLS token is discarded. The resulting patch features f_i are then ℓ_2 -normalized as

$$\hat{f}_i = \frac{f_i}{\|f_i\|_2}. \quad (7)$$

3.3.2 Drone-Only GMM Vocabulary Learning. A Gaussian mixture model (GMM) with K components is fitted to the normalized drone patch features $X_{\text{drone}} = \{\hat{f}_i\}$ using the EM algorithm [4]:

$$p(\hat{f} | \Theta) = \sum_{k=1}^K \pi_k \mathcal{N}(\hat{f} | \mu_k, \sigma_k^2). \quad (8)$$

This GMM defines the visual vocabulary and remains fixed during testing. Satellite features are never used for vocabulary learning, meaning that the representation is *satellite-free* on the vocabulary side. Therefore, although the same frozen DINOv3 extractor is applied to both drone pseudo-orthophotos and satellite tiles, the visual vocabulary and higher-order aggregation statistics are learned exclusively from drone data. As a result, the retrieval space is satellite-free during training and effectively induced by the drone domain.

3.3.3 Fisher Vector Aggregation and Cross-View Retrieval. The patch features of each image are aggregated into a Fisher vector [28]. Let N denote the number of patches in an image and let y_{ik} be the posterior probability of component k for patch i . The first- and second-order Fisher gradients are given by

$$G_{\mu_k} = \frac{1}{N\sqrt{\pi_k}} \sum_{i=1}^N y_{ik} \frac{\hat{f}_i - \mu_k}{\sigma_k}, \quad (9)$$

$$G_{\sigma_k^2} = \frac{1}{N\sqrt{2\pi_k}} \sum_{i=1}^N y_{ik} \left[\frac{(\hat{f}_i - \mu_k)^2}{\sigma_k^2} - 1 \right], \quad (10)$$

where all divisions and squares are element-wise. The resulting gradients are concatenated across all K components and power-normalized, followed by ℓ_2 normalization, to form the global descriptor g .

At test time, both UAV-side pseudo-orthophotos g_{drone} and satellite tiles g_{sat} are encoded using the same DINOv3+GMM+Fisher pipeline, and their similarity is measured by cosine similarity:

$$s(g_{\text{drone}}, g_{\text{sat}}) = g_{\text{drone}}^\top g_{\text{sat}}. \quad (11)$$

Retrieval is then performed by ranking the gallery descriptors in descending order of similarity. See supplementary material D for details.

4 Experiments

4.1 Datasets and Evaluation Protocol

University-1652 [42] contains 701 locations with drone, ground, and satellite imagery, totaling over 50k images. Its dense multi-view coverage around each building makes it a standard DVGL

benchmark. We follow the original split and use the drone and satellite subsets for cross-view retrieval.

SUES-200 [46] includes 200 locations with multi-altitude drone images and satellite views. We use SUES-200 mainly to test generalization across flight heights.

Protocol. Following most prior works [5, 29, 32], we report Recall@1 (R@1) and Average Precision (AP) for both Drone→Satellite and Satellite→Drone retrieval.

Query Protocol and Comparison Scope. Our method is designed for UAV-sequence-based 3D reconstruction and therefore represents each UAV-side location using the multi-view UAV observations available at that location. Specifically, the UAV-side representation is the pseudo-orthophoto reconstructed from the corresponding multi-view UAV sequence. Under this setting, the primary and protocol-matched comparison should be made against reproduced generalization baselines evaluated under the same multi-view UAV information budget. For these baselines, we use exactly the same multi-view UAV observations, extract one descriptor from each UAV view, and average them into a single location-level representation. By contrast, the supervised and unsupervised/self-supervised DVGL results are quoted from the original papers and typically follow different evaluation protocols, most commonly single-image UAV queries, while also using satellite imagery during training. Hence, these methods are reported only as contextual references rather than as strictly protocol-matched baselines, and the main conclusion of our experiments should be drawn from the comparison with the reproduced generalization baselines.

4.2 Implementation Details

All experiments are conducted on a single NVIDIA RTX 4090D GPU. For each drone scene, we reconstruct a 3DGS model with the official implementation [15], using COLMAP [27] for initialization and default hyper-parameters for optimization. We then sample a dense point cloud, estimate the ground plane, render pseudo-orthophotos with soft-roof compositing, and apply geometry-guided inpainting plus LaMa. The pseudo-orthophoto rendering stage is performed on reconstructed scene geometry and does not require camera parameters at rendering time, although COLMAP poses are used during reconstruction and initialization. A frozen DINOv3 ViT backbone [30] provides patch features. The GMM vocabulary for Fisher vectors is trained solely on drone pseudo-orthophoto patches with $K = 256$ components unless otherwise stated.

For the reproduced generalization baselines, we use the same multi-view UAV observations as input. One descriptor is extracted from each UAV view, and the resulting view-level descriptors are averaged to obtain a single location-level representation. Unless explicitly stated, the supervised and unsupervised/self-supervised methods are reported using the numbers from their original papers.

4.3 Quantitative Evaluation

We compare our method with recent supervised [3, 5, 8, 19, 20, 31, 35, 37, 38, 43, 45] and unsupervised/self-supervised [1, 2, 18, 36] DVGL methods reported in the literature, as well as strong generalization baselines [6, 9, 10, 14, 21, 30] that we reproduce under our multi-view UAV protocol.

Table 1: Quantitative comparison on University-1652. \uparrow indicates that higher values are better. Best results in each group are highlighted in bold. Pub. and SF denote publication venue and satellite-free, respectively. Generalization baselines are reproduced under our multi-view UAV protocol using view-level average pooling, while the supervised and unsupervised/self-supervised methods are reported from the literature under their original evaluation protocols.

Model	Pub.	SF	D→S		S→D	
			R@1 \uparrow	AP \uparrow	R@1 \uparrow	AP \uparrow
Supervised						
Instance Loss [43]	TOMM'2020	×	58.23	62.91	74.47	59.45
LPN [35]	TCSVT'2021	×	75.93	79.14	86.45	74.79
FSRA [3]	TCSVT'2021	×	84.51	86.71	88.45	83.37
Sample4Geo [5]	ICCV'2023	×	92.65	93.81	95.14	91.39
MFJR [8]	TGRS'2024	×	91.87	93.15	95.29	91.51
Safe-Net [19]	TIP'2024	×	86.98	88.85	91.22	86.06
MFRGN [37]	ACMMM'2024	×	93.18	63.95	72.19	62.28
CDM-Net [45]	TGRS'2025	×	95.13	96.04	96.68	94.05
CGSI [31]	TCSVT'2025	×	95.45	96.10	96.58	95.36
WeatherPrompt [38]	NeurIPS'2025	×	82.78	85.18	89.16	81.80
DiffusionUavLoc [20]	IOT'2026	×	94.10	95.93	98.14	97.83
Unsupervised / Self-Supervised						
EM-CVGL [18]	TGRS'2024	×	70.29	74.93	79.03	61.03
CDIKTNet [1]	arXiv'2025	×	83.30	85.73	87.73	76.53
Wang [36]	AAAI'2025	×	85.95	90.33	94.01	82.66
DMNIL [2]	arXiv'2025	×	90.17	91.67	95.01	88.95
Generalization						
ResNet-50 [10]	CVPR'2016	✓	6.25	8.43	28.39	7.20
ViT-Base [6]	ICLR'2021	✓	8.90	11.23	28.53	11.08
ConvNeXt-Base [21]	CVPR'2022	✓	15.00	18.13	39.66	19.80
AnyLoc [14]	RA-L'2023	✓	34.36	42.32	42.74	38.72
DINOv3 [30]	arXiv'2025	✓	31.25	40.67	46.48	37.91
MambaVision [9]	CVPR'2025	✓	5.04	7.04	21.40	6.30
Ours	–	✓	62.05	67.59	51.07	57.08

4.3.1 Results on the University-1652 Dataset. Tab. 1 reports the results on University-1652. As expected, supervised and self-supervised methods that use satellite imagery during training achieve the highest absolute performance. In particular, recent supervised approaches such as CGSI [31], CDM-Net [45], and DiffusionUavLoc [20] reach above 94% R@1 in at least one retrieval direction, while the strongest self-supervised baseline, DMNIL [2], also delivers strong performance with 90.17% R@1 for Drone→Satellite and 95.01% R@1 for Satellite→Drone.

Under the Satellite-Free Learning setting, however, our method still clearly outperforms all generalization-only baselines. For Drone→Satellite retrieval, we obtain 62.05% R@1 and 67.59% AP, which substantially exceeds AnyLoc (34.36% / 42.32%), DINOv3 (31.25% / 40.67%), and all other generalization baselines. For Satellite→Drone retrieval, we achieve 51.07% R@1 and 57.08% AP, again surpassing the strongest generalization competitors, including DINOv3 (46.48% / 37.91%) and AnyLoc (42.74% / 38.72%). These results confirm that explicit 3D viewpoint normalization and drone-only Fisher

Table 2: Performance comparison on SUES-200 across four drone flight altitudes for both Drone→Satellite (D→S) and Satellite→Drone (S→D) retrieval. Bold numbers indicate the best result for each metric at each altitude within the same learning type and retrieval direction. “Pub.” and “SF” denote publication venue and satellite-free, respectively. Generalization baselines are reproduced under our multi-view UAV protocol using view-level average pooling, while the supervised and unsupervised/self-supervised methods are reported from the literature under their original protocols.

Model	Pub.	SF	150 m				200 m				250 m				300 m			
			D→S		S→D		D→S		S→D		D→S		S→D		D→S		S→D	
			R@1↑	AP↑	R@1↑	AP↑	R@1↑	AP↑	R@1↑	AP↑	R@1↑	AP↑	R@1↑	AP↑	R@1↑	AP↑	R@1↑	AP↑
Supervised																		
SUES baseline [46]	TOMM'2020	×	59.32	64.93	82.50	58.95	62.30	67.24	85.00	62.56	71.35	75.49	88.75	69.96	77.17	80.67	96.25	84.16
LPN [35]	TCSVT'2021	×	61.58	67.23	83.75	66.78	70.85	75.96	88.75	75.01	80.38	83.80	92.50	81.34	81.47	84.53	92.50	85.72
FSRA [3]	TCSVT'2021	×	68.25	73.45	83.75	76.67	83.00	85.99	90.00	85.34	90.68	92.27	93.75	90.17	91.95	91.95	95.00	92.03
Sample4Geo [5]	ICCV'2023	×	92.60	94.00	97.50	93.63	97.38	97.81	98.75	96.70	98.28	98.64	98.75	98.28	99.18	99.36	98.75	98.05
MFJR [8]	TGRS'2024	×	88.95	91.05	95.00	89.31	93.60	94.72	96.25	94.69	95.42	96.28	97.50	96.92	97.45	97.84	98.75	97.14
Safe-Net [19]	TIP'2024	×	81.05	84.76	97.50	86.36	91.10	93.04	96.25	92.61	94.52	95.74	97.50	94.98	94.57	95.60	98.75	95.57
MFRGN [37]	ACMMM'2024	×	95.18	96.14	98.75	90.48	97.95	98.38	100.00	96.64	98.95	99.13	100.00	99.25	99.53	99.62	100.00	98.81
CDM-Net [45]	TGRS'2025	×	93.78	95.16	95.25	92.24	97.62	98.16	98.50	96.40	98.28	98.69	99.00	97.60	99.20	99.31	99.00	98.01
CGSI [31]	TCSVT'2025	×	95.95	96.80	97.50	96.22	97.72	98.15	98.75	97.62	97.60	98.03	98.75	98.01	97.83	98.23	98.75	97.92
WeatherPrompt [38]	NeurIPS'2025	×	74.90	78.77	80.00	68.50	80.78	83.92	83.75	77.29	86.55	89.00	91.25	82.76	89.35	91.49	92.50	86.11
DiffusionUavLoc [20]	IOT'2026	×	92.90	93.93	97.50	97.67	93.67	94.66	97.50	98.13	93.87	94.71	97.50	97.69	93.55	94.49	98.75	95.63
Unsupervised / Self-Supervised																		
EM-CVGL [18]	TGRS'2024	×	55.23	60.80	73.75	54.00	60.95	61.03	91.25	65.65	68.10	72.62	96.25	72.02	74.42	78.20	97.50	74.74
CDIKTNet [1]	arXiv'2025	×	82.75	85.25	88.75	80.33	89.35	91.13	93.75	88.17	93.15	94.39	95.00	92.15	95.18	96.12	98.75	94.37
Wang [36]	AAAI'2025	×	76.90	84.95	87.50	74.81	87.88	92.60	92.50	87.15	92.98	95.66	96.25	91.20	95.10	96.92	98.75	94.52
DMNIL [2]	arXiv'2025	×	90.98	92.66	96.25	90.05	95.03	96.14	97.50	94.80	97.45	98.03	98.75	96.82	98.23	98.64	98.75	97.33
Generalization																		
ResNet-50	CVPR'2016	✓	7.52	11.19	8.75	6.34	11.65	15.78	22.50	11.24	19.08	23.28	32.50	16.39	23.87	28.27	38.75	21.06
ViT-Base [6]	ICLR'2021	✓	14.27	19.15	21.25	9.71	19.02	23.92	28.75	16.19	24.57	29.09	46.25	26.97	27.75	32.36	58.75	33.98
ConvNeXt-Base [21]	CVPR'2022	✓	24.55	30.18	20.00	11.08	32.15	37.59	38.75	22.12	39.23	44.72	52.50	33.66	46.90	52.46	60.00	43.89
AnyLoc [14]	RA-L'2023	✓	30.00	42.74	52.50	29.06	34.00	46.74	61.23	41.24	36.78	50.41	64.23	68.42	41.00	51.97	71.90	79.56
DINOv3 [30]	arXiv'2025	✓	34.67	40.74	28.75	21.50	42.32	48.36	38.75	33.29	48.00	54.06	52.50	42.39	53.65	59.32	67.50	48.77
MambaVision [9]	CVPR'2025	✓	8.85	12.56	7.50	5.28	10.53	14.22	13.75	7.84	13.60	17.15	20.00	10.48	19.57	23.21	30.00	16.57
Ours	—	✓	78.75	81.86	78.75	63.03	82.50	85.51	88.75	80.77	88.65	90.75	95.00	88.81	93.50	94.87	97.50	92.34

aggregation provide a substantial advantage over direct feature generalization under our multi-view satellite-free protocol.

At the same time, there remains a clear gap to methods that exploit satellite imagery during training, especially recent supervised approaches such as CGSI, CDM-Net, and DiffusionUavLoc. This gap is expected, since those methods benefit from cross-view supervision or satellite participation during representation learning, whereas our pipeline is trained exclusively on drone imagery. Nevertheless, the proposed method establishes a much stronger satellite-free baseline than existing generalization-only approaches, demonstrating the practical value of our framework when satellite data are delayed, restricted, or unavailable during training.

We emphasize that the most direct and protocol-matched comparison is with the reproduced generalization baselines, since they use the same multi-view UAV observations as our method. By contrast, the supervised and unsupervised/self-supervised DVGL methods are included mainly as reference results because they follow their original evaluation protocols.

4.3.2 Results on the SUES-200 Dataset. We further evaluate our method on SUES-200 [46] under four drone flight altitudes (150 m, 200 m, 250 m, and 300 m). Table 2 summarizes the results for both

Drone→Satellite and Satellite→Drone retrieval. As with University-1652, the fairest direct comparison is with the reproduced generalization baselines under the same multi-view UAV input protocol, while the satellite-based methods serve as contextual references. Across all altitudes and in both retrieval directions, our method consistently and substantially outperforms all generalization-only baselines. For Drone→Satellite retrieval, our R@1 improves from 78.75% at 150 m to 93.50% at 300 m, whereas the strongest generalization baseline, DINOv3, reaches only 34.67%–53.65% R@1. For Satellite→Drone retrieval, our method similarly increases from 78.75% to 97.50% R@1 across altitudes, clearly surpassing both DINOv3 (28.75%–67.50%) and AnyLoc (52.50%–71.90%). The same trend is also reflected in AP, where our method consistently maintains a large margin over all generalization baselines in both directions. These results show that the proposed 3DGS-based viewpoint normalization and drone-only Fisher representation generalize robustly across different flight heights and substantially narrow the cross-view gap without using any satellite-side training data.

Compared with supervised and unsupervised/self-supervised methods that have access to satellite imagery during training, our method still lags behind in absolute performance, especially against

recent strong supervised approaches such as MFRGN [37], Sample4Geo [5], CDM-Net [45], and DiffusionUavLoc [20], as well as the self-supervised method DMNIL [2]. In particular, several supervised methods already reach near-saturated performance at medium-to-high altitudes, with R@1 often approaching or exceeding 99%. Nevertheless, under our multi-view satellite-free protocol, our method already delivers strong and stable performance across all altitudes while dramatically outperforming all generalization-only baselines. This highlights the practical value of our framework for real-world scenarios in which satellite imagery is delayed, restricted, or unavailable during training.

Additional altitude-wise visualizations of R@1 and AP on SUES-200 are provided in supplementary material E.

4.4 Qualitative Retrieval Examples

To better understand the behavior of the proposed method, we visualize qualitative retrieval results in both retrieval directions. Figure 4 shows Drone→Satellite retrieval. For each query location, the left part shows representative oblique UAV views, the middle part shows the pseudo-orthophoto generated by our 3DGS-based pipeline, and the right part presents the top-5 retrieved satellite images. In successful cases, the pseudo-orthophoto aligns scene layout and structural cues well with the satellite imagery. Road networks, block shapes, and building footprints are often consistent across views, making the retrieved matches visually intuitive. Compared with directly using oblique UAV views, the viewpoint-normalized pseudo-orthophoto reduces geometric distortion and view-dependent appearance changes, leading to cleaner and more semantically consistent cross-view matches.

Figure 5 presents Satellite→Drone retrieval. The left column shows the satellite query, while the right columns display the top-5 retrieved UAV pseudo-orthophotos. When retrieval succeeds, the pseudo-orthophoto faithfully preserves the global layout of the scene, such as stadium contours, waterfront outlines, or campus-scale building arrangements, even though it is reconstructed solely from UAV imagery. This further supports that the proposed 3DGS-based pseudo-orthophoto generation effectively narrows the domain gap between UAV and satellite views in both retrieval directions.

We also observe representative failure cases. In scenes with strong occlusion or large homogeneous regions, such as waterfront areas with extended water surfaces, the system may retrieve visually similar but geographically different locations. Similar confusion also occurs in densely repeated residential regions, where multiple buildings share nearly identical appearance and layout. These challenging cases suggest several promising directions for future work, including multi-scale patch modeling, additional geometric or semantic priors, and auxiliary context such as language descriptions to further disambiguate hard cross-view matches under the satellite-free training setting.

4.5 Runtime Analysis

We further analyze the runtime of the main stages in the proposed pipeline on University-1652. To reflect the practical computational cost more clearly, we divide the pipeline into geometry preprocessing and representation learning / retrieval. The former includes

Table 3: Runtime analysis of the main stages of the proposed pipeline.

Stage	Time (s)	Time (min)
COLMAP reconstruction	29.10	0.49
3DGS optimization	353.00	5.88
GMM / vocabulary learning	798.65	13.31
Feature extraction + retrieval	63.99	1.07

Table 4: Comprehensive ablation studies on University-1652. We report R@1 and AP for both Drone→Satellite and Satellite→Drone retrieval. Bold numbers indicate the best result within each ablation group.

Setting	Drone→Satellite		Satellite→Drone	
	R@1↑	AP↑	R@1↑	AP↑
Reconstruction / Rendering				
w/o 3DGS	40.23	47.10	48.80	45.32
w/o LaMa	53.92	60.36	47.50	53.11
COLMAP only	56.06	61.89	48.93	54.55
Aggregation				
VLAD	52.21	58.06	45.65	51.61
SoftVLAD ($\alpha = 10$)	46.08	51.59	35.81	41.36
SoftVLAD ($\alpha = 30$)	50.50	56.10	42.65	48.48
SoftVLAD ($\alpha = 50$)	50.36	56.02	44.22	49.85
SoftVLAD ($\alpha = 100$)	50.07	56.01	45.93	51.40
SoftVLAD ($\alpha = 200$)	52.64	58.29	49.07	54.54
Fisher ($K = 256$) (default)	62.05	67.59	51.07	57.08
Number of clusters / GMM components				
$K = 16$	49.79	55.67	44.37	50.38
$K = 32$	53.50	59.96	47.50	53.48
$K = 64$	56.49	62.68	49.36	55.33
$K = 128$	60.20	65.99	50.93	56.70
$K = 256$ (default)	62.05	67.59	51.07	57.08
$K = 512$	60.63	66.61	51.21	57.25
Descriptor subsampling				
100k	59.49	65.13	50.50	56.37
500k (default)	62.05	67.59	51.07	57.08
1000k	62.05	67.59	51.07	57.08
2000k	62.05	67.59	51.07	57.08

COLMAP reconstruction and 3DGS optimization, while the latter includes offline GMM vocabulary learning as well as test-time feature extraction and retrieval.

As shown in Table 3, COLMAP reconstruction requires only 29.10 s, whereas 3DGS optimization takes 353.00 s, indicating that the main cost of the geometry preprocessing stage comes from neural scene optimization rather than from the initial structure-from-motion step. For the representation stage, offline GMM vocabulary learning requires 798.65 s, while feature extraction and cross-view retrieval at test time take only 63.99 s. Overall, these results show that the dominant computational cost of our method lies in offline preprocessing and vocabulary construction, whereas the final retrieval stage remains relatively efficient.

4.6 Ablation Study

In the reconstruction/rendering ablations, “w/o 3DGS” removes 3DGS reconstruction, “w/o LaMa” removes large-hole completion,



Figure 4: Qualitative Drone→Satellite retrieval results. Each row corresponds to one query location. From left to right: (i) several representative raw UAV views from the multi-view query sequence, shown for visualization only; (ii) the pseudo-orthophoto reconstructed from the full UAV sequence and used as the actual query representation in our method; and (iii) the top-5 retrieved satellite images, where the correct match is highlighted in green and incorrect candidates are framed in red.



Figure 5: Qualitative Satellite→Drone retrieval results. Each row shows a satellite query on the left and the top-5 retrieved drone pseudo-orthophotos on the right, with correct matches highlighted in green and incorrect ones framed in red.

and “COLMAP only” replaces 3DGS with COLMAP-based geometry for pseudo-orthophoto generation.

Effectiveness of 3DGS-based reconstruction and rendering.

The first group of ablations verifies the importance of the proposed 3D reconstruction and rendering pipeline. Removing 3DGS causes the largest performance drop, reducing Drone→Satellite from 62.05% / 67.59% to 40.23% / 47.10% in terms of R@1/AP, and Satellite→Drone from 51.07% / 57.08% to 48.80% / 45.32%. This confirms that explicit 3D reconstruction and pseudo-orthophoto generation are essential for narrowing the severe viewpoint gap between oblique UAV views and satellite imagery. Removing LaMa also degrades performance, especially for Drone→Satellite, indicating that texture completion and structural consistency are beneficial for robust cross-view matching. Using COLMAP only yields better results than the variants without 3DGS or without LaMa, but still remains clearly below the full model. This suggests that dense

geometry alone is insufficient, and that the combination of 3DGS-based rendering and geometry-aware completion is important for obtaining discriminative pseudo-orthophotos.

Effectiveness of Fisher vector aggregation. The second group evaluates different aggregation strategies. Fisher vector aggregation consistently outperforms VLAD and all SoftVLAD variants. In particular, Fisher with $K=256$ achieves the best overall performance, reaching 62.05% / 67.59% for Drone→Satellite and 51.07% / 57.08% for Satellite→Drone. By comparison, standard VLAD only obtains 52.21% / 58.06% and 45.65% / 51.61%, respectively. The SoftVLAD variants remain consistently below Fisher across all tested settings of α . These results indicate that higher-order Fisher statistics are more effective than first-order residual aggregation for modeling the distribution of DINOv3 patch descriptors in the satellite-free setting.

Effect of the number of GMM components. We further study the influence of the vocabulary size by varying the number of GMM components. As K increases from 16 to 256, retrieval accuracy improves steadily in both directions, showing that a larger visual vocabulary provides a more expressive partitioning of the feature space. For example, Drone→Satellite R@1 rises from 49.79% at $K=16$ to 62.05% at $K=256$, while Satellite→Drone improves from 44.37% to 51.07%. Increasing the size further to $K=512$ does not bring additional benefits, suggesting that the gains saturate once the vocabulary is sufficiently fine-grained. Overall, $K=256$ provides the best tradeoff between expressiveness and performance in our setting.

Effect of descriptor subsampling. Finally, we examine the impact of the number of sampled patch descriptors used for vocabulary learning. Increasing the number of descriptors from 100k to 500k noticeably improves performance, while further scaling to 1000k and 2000k yields no additional gains. This shows that the proposed representation is relatively stable once the descriptor pool is sufficiently large, and that 500k samples already provide

enough coverage of the drone feature distribution for reliable GMM estimation.

5 Conclusion

In this paper, we propose a satellite-free training framework for drone-view geo-localization, where no satellite imagery is used in downstream task-specific training. By leveraging 3D Gaussian Splatting to reconstruct dense UAV scenes and generate geometry-based pseudo-orthophotos, our method converts multi-view drone observations into cross-view compatible UAV-side representations. A frozen DINOv3 backbone combined with GMM-based Fisher vector aggregation enables representation learning solely from drone data. Experimental results on University-1652 and SUES-200 demonstrate strong performance under the satellite-free setting, substantially outperforming reproduced generalization baselines and narrowing the gap to methods that use satellite imagery during training. We hope this work provides a practical foundation for drone-view geo-localization when satellite imagery is unavailable, and offers insights for future improvements such as more efficient 3D reconstruction and the incorporation of temporal or semantic priors.

References

- [1] Zhongwei Chen, Zhao-Xu Yang, Hai-Jun Rong, and Jiawei Lang. 2025. From Limited Labels to Open Domains: An Efficient Learning Paradigm for UAV-view Geo-Localization. *arXiv preprint arXiv:2503.07520* (2025).
- [2] Zhongwei Chen, Zhao-Xu Yang, Hai-Jun Rong, and Guoqi Li. 2025. Without Paired Labeled Data: End-to-End Self-Supervised Learning for Drone-view Geo-Localization. *arXiv preprint arXiv:2502.11381* (2025).
- [3] Ming Dai, Jianhong Hu, Jiedong Zhuang, and Enhui Zheng. 2021. A transformer-based feature segmentation and region alignment method for UAV-view geo-localization. *IEEE Transactions on Circuits and Systems for Video Technology* 32, 7 (2021), 4376–4389.
- [4] Arthur P Dempster, Nan M Laird, and Donald B Rubin. 1977. Maximum likelihood from incomplete data via the EM algorithm. *Journal of the royal statistical society: series B (methodological)* 39, 1 (1977), 1–22.
- [5] Fabian Deuser, Konrad Habel, and Norbert Oswald. 2023. Sample4geo: Hard negative sampling for cross-view geo-localisation. In *Proceedings of the IEEE/CVF International Conference on Computer Vision*. 16847–16856.
- [6] Alexey Dosovitskiy. 2020. An image is worth 16x16 words: Transformers for image recognition at scale. *arXiv preprint arXiv:2010.11929* (2020).
- [7] Martin A Fischler and Robert C Bolles. 1981. Random sample consensus: a paradigm for model fitting with applications to image analysis and automated cartography. *Commun. ACM* 24, 6 (1981), 381–395.
- [8] Fawei Ge, Yunzhou Zhang, Li Wang, Wei Liu, Yixiu Liu, Sonya Coleman, and Dermot Kerr. 2024. Multilevel feedback joint representation learning network based on adaptive area elimination for cross-view geo-localization. *IEEE transactions on geoscience and remote sensing* 62 (2024), 1–15.
- [9] Ali Hatamizadeh and Jan Kautz. 2025. Mambavision: A hybrid mamba-transformer vision backbone. In *Proceedings of the Computer Vision and Pattern Recognition Conference*. 25261–25270.
- [10] Kaiming He, Xiangyu Zhang, Shaoqing Ren, and Jian Sun. 2016. Deep residual learning for image recognition. In *Proceedings of the IEEE conference on computer vision and pattern recognition*. 770–778.
- [11] Alex Horton and Siobhán O’Grady. 2025. U.S. suspends commercial satellite imagery service to Ukraine. The Washington Post. <https://www.washingtonpost.com/national-security/2025/03/07/maxar-ukraine-satellite-imagery/>
- [12] Arnold Irschara, Christopher Zach, Jan-Michael Frahm, and Horst Bischof. 2009. From structure-from-motion point clouds to fast location recognition. In *2009 IEEE Conference on Computer Vision and Pattern Recognition*. IEEE, 2599–2606.
- [13] Howoong Jun, Hyeonwoo Yu, and Songhwa Oh. 2024. Renderable street view map-based localization: Leveraging 3d gaussian splatting for street-level positioning. In *2024 IEEE/RISJ International Conference on Intelligent Robots and Systems (IROS)*. IEEE, 5635–5640.
- [14] Nikhil Keetha, Avneesh Mishra, Jay Karhade, Krishna Murthy Jatavallabhula, Sebastian Scherer, Madhava Krishna, and Sourav Garg. 2023. Anyloc: Towards universal visual place recognition. *IEEE Robotics and Automation Letters* 9, 2 (2023), 1286–1293.
- [15] Bernhard Kerbl, Georgios Kopanas, Thomas Leimkühler, and George Drettakis. 2023. 3D Gaussian splatting for real-time radiance field rendering. *ACM Trans. Graph.* 42, 4 (2023), 139–1.
- [16] Guopeng Li, Ming Qian, and Gui-Song Xia. 2024. Unleashing unlabeled data: A paradigm for cross-view geo-localization. In *Proceedings of the IEEE/CVF Conference on Computer Vision and Pattern Recognition*. 16719–16729.
- [17] Haoyuan Li, Chang Xu, Wen Yang, Li Mi, Huai Yu, Haijian Zhang, and Gui-Song Xia. 2025. Unsupervised Multi-view UAV Image Geo-localization via Iterative Rendering. *IEEE Transactions on Geoscience and Remote Sensing* (2025).
- [18] Haoyuan Li, Chang Xu, Wen Yang, Huai Yu, and Gui-Song Xia. 2024. Learning cross-view visual geo-localization without ground truth. *IEEE Transactions on Geoscience and Remote Sensing* (2024).
- [19] Jinliang Lin, Zhiming Luo, Dazhen Lin, Shaozi Li, and Zhun Zhong. 2024. A self-adaptive feature extraction method for aerial-view geo-localization. *IEEE Transactions on Image Processing* (2024).
- [20] Tao Liu, Kan Ren, and Qian Chen. 2026. DiffusionUavLoc: Visually Prompted Diffusion for Cross-View UAV Localization. *IEEE Internet of Things Journal* (2026).
- [21] Zhuang Liu, Hanzi Mao, Chao-Yuan Wu, Christoph Feichtenhofer, Trevor Darrell, and Saining Xie. 2022. A convnet for the 2020s. In *Proceedings of the IEEE/CVF conference on computer vision and pattern recognition*. 11976–11986.
- [22] Haitao Lu, Haijier Chen, Haoze Liu, Shoujian Zhang, Bo Xu, and Ziao Liu. 2025. 3DGS_LSR: Large_Scale Relocation for Autonomous Driving Based on 3D Gaussian Splatting. *arXiv preprint arXiv:2507.05661* (2025).
- [23] Ben Mildenhall, Pratul P Srinivasan, Matthew Tancik, Jonathan T Barron, Ravi Ramamoorthi, and Ren Ng. 2021. Nerf: Representing scenes as neural radiance fields for view synthesis. *Commun. ACM* 65, 1 (2021), 99–106.
- [24] Arthur Moreau, Nathan Piasco, Dzmitry Tsishkou, Bogdan Stanculescu, and Arnaud de La Fortelle. 2022. Lens: Localization enhanced by nerf synthesis. In *Conference on Robot Learning*. PMLR, 1347–1356.
- [25] Illia Novikov and Jon Gambrell. 2025. Russia attacks Ukraine’s energy supplies as US cuts its access to satellite images. AP News. <https://apnews.com/article/942d5fa7c9bdd42e6361e5fa7ddb3ae3>
- [26] Maxime Oquab, Timothée Darcet, Théo Moutakanni, Huy Vo, Marc Szafraniec, Vasil Khalidov, Pierre Fernandez, Daniel Haziza, Francisco Massa, Alaaeldin El-Nouby, et al. 2023. Dinov2: Learning robust visual features without supervision. *arXiv preprint arXiv:2304.07193* (2023).
- [27] Linfei Pan, Dániel Baráth, Marc Pollefeys, and Johannes L Schönberger. 2024. Global structure-from-motion revisited. In *European Conference on Computer Vision*. Springer, 58–77.
- [28] Florent Perronnin, Jorge Sánchez, and Thomas Mensink. 2010. Improving the fisher kernel for large-scale image classification. In *European conference on computer vision*. Springer, 143–156.
- [29] Tianrui Shen, Yingmei Wei, Lai Kang, Shanshan Wan, and Yee-Hong Yang. 2023. MCCG: A ConvNeXt-based multiple-classifier method for cross-view geo-localization. *IEEE Transactions on Circuits and Systems for Video Technology* 34, 3 (2023), 1456–1468.
- [30] Oriane Siméoni, Huy V Vo, Maximilian Seitzer, Federico Baldassarre, Maxime Oquab, Cijo Jose, Vasil Khalidov, Marc Szafraniec, Seungeun Yi, Michaël Ramamonjisoa, et al. 2025. Dinov3. *arXiv preprint arXiv:2508.10104* (2025).
- [31] Jian Sun, Junlang Huang, Xinyu Jiang, Yimin Zhou, and Chi-Man VONG. 2025. CGSI: Context-Guided and UAV’s Status Informed Multimodal Framework for Generalizable Cross-View Geo-Localization. *IEEE Transactions on Circuits and Systems for Video Technology* (2025).
- [32] Jian Sun, Hao Sun, Lin Lei, Kefeng Ji, and Gangyao Kuang. 2024. TirSA: A three stage approach for UAV-satellite cross-view geo-localization based on self-supervised feature enhancement. *IEEE Transactions on Circuits and Systems for Video Technology* 34, 9 (2024), 7882–7895.
- [33] Roman Suvorov, Elizaveta Logacheva, Anton Mashikhin, Anastasia Remizova, Arsenii Ashukha, Aleksei Silvestrov, Naejin Kong, Harshith Goka, Kiwoong Park, and Victor Lempitsky. 2022. Resolution-robust large mask inpainting with fourier convolutions. In *Proceedings of the IEEE/CVF winter conference on applications of computer vision*. 2149–2159.
- [34] Alexandru Telea. 2004. An image inpainting technique based on the fast marching method. *Journal of graphics tools* 9, 1 (2004), 23–34.
- [35] Tingyu Wang, Zhedong Zheng, Chenggang Yan, Jiyong Zhang, Yaoqi Sun, Bolun Zheng, and Yi Yang. 2021. Each part matters: Local patterns facilitate cross-view geo-localization. *IEEE Transactions on Circuits and Systems for Video Technology* 32, 2 (2021), 867–879.
- [36] Xueyi Wang, Lele Zhang, Zheng Fan, Yang Liu, Chen Chen, and Fang Deng. 2025. From Coarse to Fine: A Matching and Alignment Framework for Unsupervised Cross-View Geo-Localization. In *Proceedings of the AAAI Conference on Artificial Intelligence*, Vol. 39. 8024–8032.
- [37] Yuntao Wang, Jinpu Zhang, Ruonan Wei, Wenbo Gao, and Yuehuan Wang. 2024. Mfign: Multi-scale feature representation generalization network for ground-to-aerial geo-localization. In *Proceedings of the 32nd ACM International Conference on Multimedia*. 2574–2583.

Table 5: Hyperparameters used in our implementation. We list parameters that are tightly coupled to our method and explicitly fixed in code.

(a) 3DGS optimization and Gaussian field		
Symbol	Description	Value
N_{iter}	Optimization steps per scene	7,000
N_p^{target}	Target points in point cloud	10^7
τ_M	Mahalanobis distance threshold	2.0
v_{min}	Minimum visibility threshold	0.05
α_{min}	Minimum Gaussian opacity	0.0
(b) Projection to pseudo-orthophotos		
Symbol	Description	Value
δ_{RANSAC}	Ground-plane inlier threshold	0.30 m
N_{pix}^{max}	Max pixels of orthographic canvas	10^8
r	Grid resolution search range	[0.0075, 0.05] m/px
ρ_{target}	Target point density per pixel	1.5 pts/px
h_{band}	Ground height bandwidth	0.18 m
h_{roof}	Minimum roof height	Adaptive
Δh_{bw}	Roof height bandwidth	0.25 m
T_{roof}	Temperature for height weights	0.125
N_{min}^{roof}	Min points per roof pixel	3
r_{roof}, r_{ground}	Splat radius (roof/ground)	1 px / 1 px
SSAA	Spatial super-sampling factor	$\times 2$
(c) Impainting		
Symbol	Description	Value
S_{small}	Max area of Telea-filled holes	12 pixels
k_{KNN}	KNN neighbors for filling	6
r_{KNN}^{max}	Max KNN search radius	4 pixels
m_{crop}	Border ratio for center-crop	0.20
(d) Feature aggregation		
Symbol	Description	Value
Backbone	DINOv3 backbone	ViT
K	GMM components	256
N_{GMM}	Sampled patch descriptors for GMM	500,000

- [38] Jiahao Wen, Hang Yu, and Zhedong Zheng. 2025. WeatherPrompt: Multi-modality Representation Learning for All-Weather Drone Visual Geo-Localization. In *NeurIPS*.
- [39] Jian Yang, David Zhang, Alejandro F Frangi, and Jing-yu Yang. 2004. Two-dimensional PCA: a new approach to appearance-based face representation and recognition. *IEEE transactions on pattern analysis and machine intelligence* 26, 1 (2004), 131–137.
- [40] Patricia Zengerle. 2025. US government revokes some access to satellite imagery for Ukraine. Reuters. <https://www.reuters.com/world/us-aerospace-firm-maxar-disables-satellite-photos-ukraine-2025-03-07/> Reporting by Patricia Zengerle; Editing by Daniel Wallis.
- [41] Zichao Zhang, Torsten Sattler, and Davide Scaramuzza. 2021. Reference pose generation for long-term visual localization via learned features and view synthesis. *International Journal of Computer Vision* 129, 4 (2021), 821–844.
- [42] Zhedong Zheng, Yunchao Wei, and Yi Yang. 2020. University-1652: A multi-view multi-source benchmark for drone-based geo-localization. In *Proceedings of the 28th ACM international conference on Multimedia*. 1395–1403.
- [43] Zhedong Zheng, Liang Zheng, Michael Garrett, Yi Yang, Mingliang Xu, and Yi-Dong Shen. 2020. Dual-path convolutional image-text embeddings with instance loss. *ACM Transactions on Multimedia Computing, Communications, and Applications (TOMM)* 16, 2 (2020), 1–23.
- [44] Qunjie Zhou, Maxim Maximov, Or Litany, and Laura Leal-Taixé. 2024. The perfect match: Exploring nerf features for visual localization. In *European Conference on Computer Vision*. Springer, 108–127.
- [45] Xin Zhou, Xuerong Yang, and Yanchun Zhang. 2025. Cdm-net: A framework for cross-view geo-localization with multimodal data. *IEEE Transactions on Geoscience and Remote Sensing* (2025).
- [46] Runzhe Zhu, Ling Yin, Mingze Yang, Fei Wu, Yuncheng Yang, and Wenbo Hu. 2023. SUES-200: A multi-height multi-scene cross-view image benchmark across drone and satellite. *IEEE Transactions on Circuits and Systems for Video Technology* 33, 9 (2023), 4825–4839.

A Details of 3DGS Reconstruction and Point-Cloud Conversion

This appendix describes the implementation of the 3DGS [15] reconstruction and the conversion from Gaussians to a dense colored point cloud, corresponding to Sec. 3.2.1 in the main paper. The main hyperparameters are summarized in Table 5(a).

3DGS optimization. Given a multi-view drone image sequence $\{I_m\}_{m=1}^M$ of a single scene, we first run COLMAP [27] to obtain camera poses $\{T_m\}$ and a COLMAP dense point cloud (used only for initialization and diagnostics). We then optimize a 3DGS scene using the official implementation, starting from the reconstructed structure. Each scene is optimized for $N_{iter} = 7,000$ steps (Table 5(a)), with standard per-iteration view and pixel sampling as in [15].

The optimized scene is represented as a set of Gaussians:

$$G = \{g_i\}_{i=1}^{N_g}, \quad g_i = (\boldsymbol{\mu}_i, \Sigma_i, \alpha_i, \mathbf{c}_i). \quad (\text{A.1})$$

where $\boldsymbol{\mu}_i \in \mathbb{R}^3$ is the 3D center, $\Sigma_i \in \mathbb{R}^{3 \times 3}$ the anisotropic covariance, $\alpha_i \in [0, 1]$ the opacity, and \mathbf{c}_i the spherical-harmonic color coefficients used by the renderer.

Visibility accumulation and pruning. To approximate which Gaussians contribute significantly to the rendered views, we accumulate a per-Gaussian visibility vector $\mathbf{v}_i \in \mathbb{R}^M$ by sampling the 3DGS renderer at a small number of views per iteration and recording whether g_i contributes non-negligible opacity to any pixel in each view. At the end of optimization, we convert this vector into a scalar visibility score by

$$v_i = \|\mathbf{v}_i\|_1 / M, \quad (\text{A.2})$$

which lies approximately in $[0, 1]$ after normalization. Gaussians with either low opacity or low visibility are discarded:

$$\alpha_i < \alpha_{min} \quad \text{OR} \quad v_i < v_{min}, \quad (\text{A.3})$$

where we set $\alpha_{min} = 0.0$ and $v_{min} = 0.05$ (Table 5(a)), keeping even weak Gaussians as long as they are repeatedly visible. We still denote the pruned set of Gaussians by G for simplicity.

Importance scores and sample allocation. We convert G into a dense colored point cloud \mathcal{P} by importance-weighted sampling. For each retained Gaussian, we define an unnormalized importance:

$$\tilde{w}_i = \alpha_i v_i, \quad (\text{A.4})$$

combining opacity and visibility. These scores are normalized over G to obtain

$$w_i^{imp} = \frac{\tilde{w}_i}{\sum_{k:g_k \in G} \tilde{w}_k}, \quad (\text{A.5})$$

which are then used to allocate the number of samples per Gaussian. Given a global target number of points $N_p^{target} = 10^7$ (Table 5(a)), we assign

$$N_i = \max(1, \lfloor N_p^{target} \cdot w_i^{imp} \rfloor). \quad (\text{A.6})$$

This ensures that high-importance Gaussians contribute more points while every retained Gaussian is represented by at least one sample.

Sampling inside anisotropic Gaussians. For each Gaussian g_i , we sample 3D positions inside its ellipsoidal support under a Mahalanobis constraint. We factor the covariance as

$$\Sigma_i = \mathbf{R}_i \Lambda_i \mathbf{R}_i^\top, \quad (\text{A.7})$$

where $\Lambda_i = \text{diag}(\lambda_{i,1}, \lambda_{i,2}, \lambda_{i,3})$ contains eigenvalues and \mathbf{R}_i the corresponding orthonormal eigenvectors. To draw a sample, we first sample a vector $\mathbf{z} \in \mathbb{R}^3$ from a truncated standard normal distribution with $\|\mathbf{z}\|_2 \leq \tau_M$, where $\tau_M = 2.0$ is the Mahalanobis distance threshold in Table 5(a). We then map \mathbf{z} to world coordinates via

$$\mathbf{x} = \boldsymbol{\mu}_i + \mathbf{R}_i \Lambda_i^{1/2} \mathbf{z}, \quad (\text{A.8})$$

so that the Mahalanobis distance

$$d_M(\mathbf{x}) = \sqrt{(\mathbf{x} - \boldsymbol{\mu}_i)^\top \Sigma_i^{-1} (\mathbf{x} - \boldsymbol{\mu}_i)} \quad (\text{A.9})$$

is guaranteed to be at most τ_M . This directly corresponds to the constraint in the main paper.

Color and normals for samples. Each sampled position \mathbf{p}_j from Gaussian g_i is assigned a color \mathbf{c}_j and surface normal \mathbf{n}_j :

- **Color.** We evaluate the SH coefficients c_i using the viewing direction corresponding to \mathbf{p}_j and a canonical camera direction (e.g., vertical), resulting in an RGB color that matches the 3DGS appearance. For efficiency and stability, we approximate this by evaluating SH at a small fixed set of canonical directions and averaging the resulting RGB values. This fixed scheme is used in all our experiments.
- **Normal.** We define the normal as the eigenvector associated with the smallest eigenvalue of Σ_i , i.e., the direction of minimal variance, which typically corresponds to the local surface normal.

Collecting all sampled points yields the final colored point cloud

$$\mathcal{P} = \{(\mathbf{p}_j, \mathbf{c}_j, \mathbf{n}_j)\}_{j=1}^{N_p}, \quad (\text{A.10})$$

where $N_p \approx N_p^{\text{target}}$ up to rounding and pruning.

B Details of PCA-Based Ground Plane and Soft-Roof Rendering

This appendix fleshes out the pseudo-orthophoto rendering from the dense point cloud \mathcal{P} described in the main paper. The key hyperparameters are given in Table 5(b).

Ground-plane estimation and local frame. We estimate the dominant ground plane π using RANSAC [7] on \mathcal{P} . We run Open3D’s `segment_plane` with distance threshold $\delta_{\text{RANSAC}} = 0.30$ m, RANSAC sample size 3, and 1000 iterations, yielding a plane

$$ax + by + cz + d = 0 \quad (\text{B.1})$$

with normal $\mathbf{n} = (a, b, c)$ and a set of inlier points treated as ground. To stabilize the in-plane directions, we perform PCA [39] on the ground inliers and use the first two principal components as a data-driven approximation of the ground axes. We then construct an orthonormal frame $(\hat{\mathbf{n}}, \mathbf{u}, \mathbf{v})$ by normalizing $\hat{\mathbf{n}} = \mathbf{n}/\|\mathbf{n}\|_2$ and setting \mathbf{u}, \mathbf{v} either from the PCA directions or, if PCA is disabled, by projecting a canonical axis onto the plane to obtain \mathbf{u} and taking $\mathbf{v} = \hat{\mathbf{n}} \times \mathbf{u}$.

Let $\bar{\mathbf{p}}$ be the mean of all projected points. Each point \mathbf{p}_j in \mathcal{P} is mapped to local coordinates

$$\begin{aligned} u_j &= (\mathbf{p}_j - \bar{\mathbf{p}})^\top \mathbf{u}, \\ v_j &= (\mathbf{p}_j - \bar{\mathbf{p}})^\top \mathbf{v}, \\ h_j &= (\mathbf{p}_j - \bar{\mathbf{p}})^\top \hat{\mathbf{n}}, \end{aligned} \quad (\text{B.2})$$

so that h_j measures height above the estimated ground plane. If the majority of off-plane points have negative heights, we flip $\hat{\mathbf{n}}$ and all h_j to enforce “roofs are positive.”

Adaptive raster resolution and canvas size. We render onto a regular grid in the (u, v) -plane. To choose the grid resolution r in meters per pixel, we:

- (1) Select points within the ground band $|h_j| \leq h_{\text{band}}$ with $h_{\text{band}} = 0.18$ m (Table 5(b)). If fewer than 50 points meet this, we fall back to all points.
- (2) Compute the bounding box widths w_x and w_y of the selected points in (u, v) and define the area $A = w_x w_y$.
- (3) Let N_{pts} be the number of selected points. We target an average density of $\rho_{\text{target}} = 1.5$ points per pixel, so the desired number of pixels is $N_{\text{pix}}^{\text{target}} = N_{\text{pts}} / \rho_{\text{target}}$.
- (4) The initial resolution is

$$r = \sqrt{\frac{A}{N_{\text{pix}}^{\text{target}}}}. \quad (\text{B.3})$$

It is clipped to the range $r \in [0.0075, 0.05]$ m/px as in Table 5(b).

- (5) The canvas width and height are

$$\begin{aligned} W &= \lceil w_x / r \rceil + 1, \\ H &= \lceil w_y / r \rceil + 1. \end{aligned} \quad (\text{B.4})$$

If $H \cdot W > N_{\text{pix}}^{\text{max}} = 10^8$, we increase r proportionally so that $H \cdot W = N_{\text{pix}}^{\text{max}}$.

We apply spatial supersampling with SSAA×2: rendering is performed on a grid of size $(2H, 2W)$ with resolution $r/2$, then down-sampled to (H, W) via Lanczos interpolation.

Ground-layer rendering. The ground layer aggregates points near the plane. We select points with

$$-h_{\text{band}} \leq h_j \leq h_{\text{band}} \quad (\text{B.5})$$

and map them to supersampled pixel coordinates (x_j, y_j) :

$$\begin{aligned} x_j &= \left\lfloor \frac{u_j - u_{\min}}{r_{\text{ss}}} \right\rfloor, \\ y_j &= \left\lfloor \frac{v_j - v_{\min}}{r_{\text{ss}}} \right\rfloor, \end{aligned} \quad (\text{B.6})$$

where (u_{\min}, v_{\min}) is the lower-left corner of the bounding box and $r_{\text{ss}} = r/2$ under SSAA×2. We flip the vertical axis to match image coordinates.

Each ground point is splatted using a disk-shaped kernel with radius $r_{\text{ground}} = 1$ px and Gaussian weights, distributing its color to neighboring pixels. Per-pixel colors are averaged over contributing points, yielding a ground RGB image I_{ground} and a binary coverage mask.

Roof-layer selection and height statistics. We first estimate a global minimum roof height h_{roof} from the distribution of non-ground heights. Concretely, we compute low and median percentiles of the off-ground heights and set h_{roof} to a robust value in the range $[0.20, \text{median}]$ that discards low clutter while keeping building roofs. Points with $h_j \geq h_{\text{roof}}$ are considered roof candidates.

Roof candidates are mapped to pixel coordinates as above. For each pixel (x, y) receiving roof points, we compute the local roof top

$$h_{\max}(x, y) = \max_{j:(x_j, y_j)=(x, y)} h_j. \quad (\text{B.7})$$

We restrict roof points to a band below the top:

$$h_j \geq h_{\max}(x_j, y_j) - \Delta h_{\text{bw}}, \quad (\text{B.8})$$

where $\Delta h_{\text{bw}} = 0.25$ m is the roof height bandwidth.

Height-adaptive weighting and roof-layer rendering. For each roof point p_j at pixel (x_j, y_j) , the height-adaptive weight is

$$w_j^{\text{height}} = \exp\left(-\frac{(h_j - h_{\text{roof}}(x_j, y_j))^2}{2\sigma_h^2}\right), \quad (\text{B.9})$$

where we set $h_{\text{roof}}(x_j, y_j) = h_{\max}(x_j, y_j)$ and

$$\sigma_h = T_{\text{roof}} \cdot \Delta h_{\text{bw}}. \quad (\text{B.10})$$

with $T_{\text{roof}} = 0.125$ controlling the sharpness of the Gaussian around the local roof top. We splat roof points using the same kernel radius $r_{\text{roof}} = 1$ px, accumulating both weighted colors and total weights per pixel. Pixels with fewer than $N_{\min}^{\text{roof}} = 3$ contributing roof points have their roof contribution suppressed to avoid isolated artifacts.

Normalized roof colors form I_{roof} , and the normalized per-pixel roof support defines a soft roof mask $M_{\text{roof}} \in [0, 1]^{H \times W}$, which directly appears in the compositing equation in the main paper.

Final compositing. After SSAA downsampling and optional small morphological clean-up, we apply the alpha compositing:

$$I_{\text{ortho}} = M_{\text{roof}} \odot I_{\text{roof}} + (1 - M_{\text{roof}}) \odot I_{\text{ground}}, \quad (\text{B.11})$$

where \odot denotes element-wise multiplication. The result is the geometry-aligned drone pseudo-orthophoto I_{ortho} used by the subsequent modules.

C Details of Geometry-Guided and LaMa Inpainting

This appendix details the geometry-guided inpainting and LaMa completion used to obtain a texture-complete pseudo-orthophoto, corresponding to Sec. 3.2.3 in the main paper. The main hyperparameters are in Table 5(c).

Hole mask and small-hole classification. We derive an initial hole mask M_{hole} from the ground and roof rendering step: pixels with low coverage or low confidence are marked as holes. Color is used only as an optional secondary cue to exclude truly dark but valid pixels.

Connected components in M_{hole} with area at most $S_{\text{small}} = 12$ pixels are treated as small holes, while larger components are handled as large missing regions.

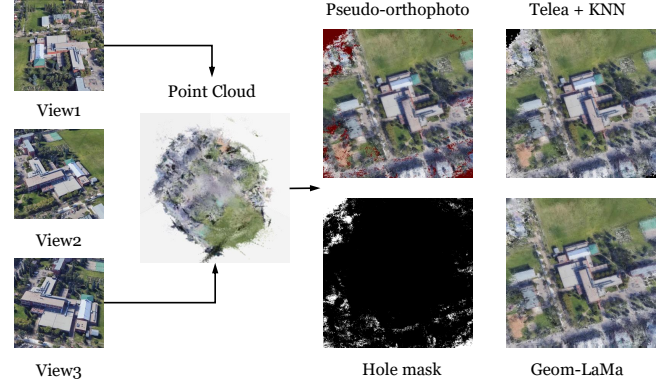


Figure 6: Illustration of the proposed geometry-guided inpainting pipeline. From left to right, three oblique drone views are used to reconstruct a dense point cloud, which is then projected into a pseudo-orthophoto together with its corresponding hole mask. We compare a purely classical inpainting strategy (Telea + KNN) with our geometry-aware LaMa completion (Geom-LaMa). The proposed Geom-LaMa variant better preserves roof contours, road boundaries, and large background regions, while effectively removing artifacts near building edges.

Morphology and classical inpainting for small holes. We first apply a light morphological closing followed by opening with a 3×3 kernel on M_{hole} to remove isolated speckles and fill tiny gaps. For each small connected component, we use OpenCV Telea [34] inpainting in RGB space, restricted to the local neighborhood of the hole. This step efficiently removes pinhole defects and small cracks without altering the underlying geometry.

For medium-sized small holes, we refine the fill by KNN-based color propagation over the (u, v) raster. Specifically, for each hole pixel, we query up to $k_{\text{KNN}} = 6$ nearest valid pixels within a maximum radius $r_{\text{KNN}}^{\max} = 4$ pixels, and interpolate colors by inverse-distance weighting. This yields a smooth, geometry-consistent fill aligned with local ground and roof structure.

LaMa completion for large holes. Holes with area exceeding S_{small} are considered large missing regions and are completed by the pre-trained LaMa network [33]. Before calling LaMa, we dilate the corresponding region in M_{hole} by a small elliptical kernel to slightly extend the mask beyond the strict boundary, so that LaMa also smooths the seam between observed and hallucinated content.

We feed the current pseudo-orthophoto and the dilated hole mask to LaMa via the simple-lama-inpainting wrapper. To preserve geometry, we restrict LaMa to background-like regions and avoid masks that cross strong roof-ground discontinuities, opting instead to shrink or split such ambiguous areas into safer subregions. LaMa operates in the (u, v) raster frame, which is already geometry-aligned, so the hallucinated content respects the global scene layout.

Geometry-guided notion. The term “geometry-guided” in the main paper refers to three aspects:

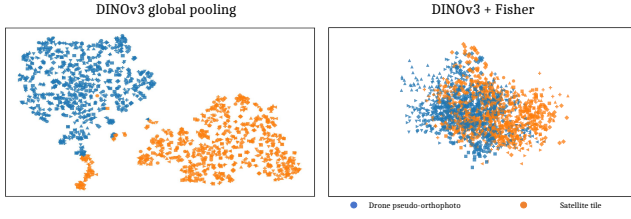


Figure 7: Embedding space comparison between different global descriptors. We visualize 2D projections of image descriptors for drone pseudo-orthophotos and satellite tiles. Left: DINOv3 with simple global pooling produces two largely separated modality clusters, revealing a strong cross-view domain gap. Right: our DINOv3+Fisher representation yields more intertwined clusters, where drone and satellite samples from similar locations lie much closer, indicating a reduced cross-view discrepancy.

- Holes are detected on the geometry-aligned pseudo-orthophoto, using coverage and height-based confidence from the 3D reconstruction.
- Classical Telea/KNN filling is performed in the local ground and roof frames on the (u, v) raster, so that diffusion and interpolation follow planar structures rather than raw perspective geometry in the original drone views.
- LaMa is used only as a last resort for large, mostly background regions. Dilated masks and restricted support prevent it from crossing major roof-ground boundaries inferred from the 3D geometry.

Center crop for retrieval. For retrieval, we store both the full inpainted pseudo-orthophoto and a center crop to reduce border artifacts. The crop is defined by removing a margin of $m_{\text{crop}} = 0.20$ of the image size on each side. This crop is tightly aligned to the (u, v) raster origin and is used as input to the DINOv3 [30]+Fisher [28] representation described in the main paper.

D Details of Satellite-Free DINOv3+Fisher Representation

This appendix provides implementation details for the satellite-free DINOv3+Fisher representation used in the main paper. The key hyperparameters are summarized in Table 5(d).

Backbone and patch extraction. We use a frozen DINOv3 ViT backbone [30] as feature extractor. For each input image, either a drone pseudo-orthophoto or a satellite tile, we:

- resize it so that the shorter side matches the ViT target size while preserving aspect ratio;
- center-crop to a fixed square resolution compatible with the backbone;
- normalize with the standard ImageNet mean and variance.

The ViT splits the image into non-overlapping patches and outputs a CLS token plus patch tokens. We discard the CLS token and keep the patch embeddings. Let D denote the embedding dimension and N the number of patches. Patch features are stacked as

$$F = [f_1, \dots, f_N]^T \in \mathbb{R}^{N \times D}. \quad (\text{D.1})$$

Each patch feature is ℓ_2 -normalized as

$$\hat{f}_i = \frac{f_i}{\|f_i\|_2}, \quad i = 1, \dots, N. \quad (\text{D.2})$$

Drone-only GMM training. To build the visual vocabulary, we collect normalized patch features from training drone images only. We uniformly sample $N_{\text{GMM}} = 500,000$ descriptors across all drone training images, with a cap per image to avoid over-representing scenes with more patches. This set is denoted by

$$X_{\text{drone}} = \{\hat{f}_i\}_{i=1}^{N_{\text{GMM}}}. \quad (\text{D.3})$$

We then fit a diagonal-covariance Gaussian mixture model with $K = 256$ components via EM [4]:

$$p(\hat{f} | \Theta) = \sum_{k=1}^K \pi_k \mathcal{N}(\hat{f} | \mu_k, \text{diag}(\sigma_k^2)), \quad (\text{D.4})$$

where π_k are mixture weights, $\mu_k \in \mathbb{R}^D$ are means, and $\sigma_k \in \mathbb{R}^D$ are per-dimension standard deviations. After convergence, the parameters

$$\Theta = \{\pi_k, \mu_k, \sigma_k\}_{k=1}^K \quad (\text{D.5})$$

are frozen and reused for both drone and satellite images at test time. Satellite patches are never used to train or adapt this vocabulary, so the representation is satellite-free on the vocabulary side.

Fisher aggregation. Given an image with normalized patch features $\{\hat{f}_i\}_{i=1}^N$, we compute posterior responsibilities

$$\gamma_{ik} = p(k | \hat{f}_i, \Theta), \quad i = 1, \dots, N, \quad k = 1, \dots, K, \quad (\text{D.6})$$

using the diagonal-covariance Gaussian likelihoods. Following the standard Fisher vector formulation [28], the gradients with respect to the means and standard deviations are

$$G_{\mu_k} = \frac{1}{N\sqrt{\pi_k}} \sum_{i=1}^N \gamma_{ik} \frac{\hat{f}_i - \mu_k}{\sigma_k}, \quad (\text{D.7})$$

$$G_{\sigma_k} = \frac{1}{N\sqrt{2\pi_k}} \sum_{i=1}^N \gamma_{ik} \left[\frac{(\hat{f}_i - \mu_k)^2}{\sigma_k^2} - 1 \right], \quad (\text{D.8})$$

where divisions, squares, and subtractions are all element-wise. Concatenating all components yields

$$G = [G_{\mu_1}; \dots; G_{\mu_K}; G_{\sigma_1}; \dots; G_{\sigma_K}] \in \mathbb{R}^{2KD}. \quad (\text{D.9})$$

Power and ℓ_2 normalization. To obtain the final descriptor g , we apply power normalization followed by ℓ_2 normalization:

$$\tilde{G} = \text{sign}(G) \odot \sqrt{|G| + \varepsilon}, \quad (\text{D.10})$$

$$g = \frac{\tilde{G}}{\|\tilde{G}\|_2}, \quad (\text{D.11})$$

where ε is a small constant and \odot is element-wise multiplication. No additional PCA or whitening is applied.

Cross-view retrieval. For each satellite tile in the gallery, we pre-compute its descriptor g_{sat} once and store it. At test time, each drone pseudo-orthophoto is encoded into g_{drone} via the same DINOv3+GMM+Fisher pipeline. Similarity is measured by cosine:

$$s(g_{\text{drone}}, g_{\text{sat}}) = g_{\text{drone}}^\top g_{\text{sat}}. \quad (\text{D.12})$$

Retrieval is performed by ranking all gallery descriptors in descending order of similarity. For large galleries, we use an inner-product

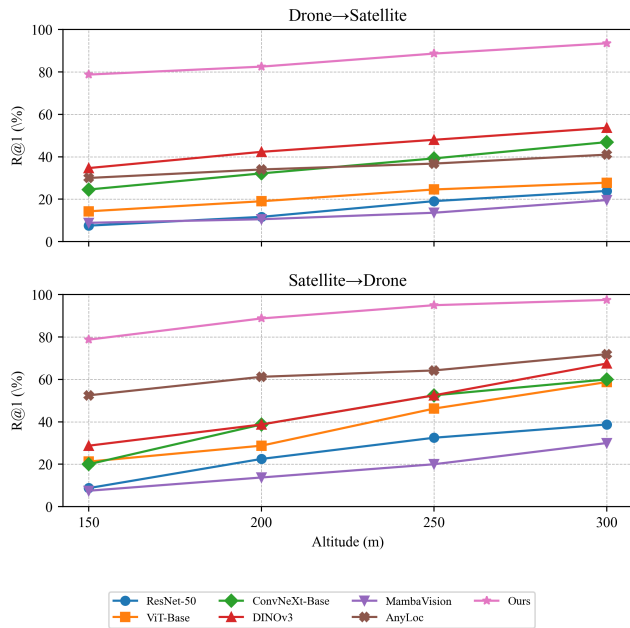


Figure 8: R@1 as a function of drone flight altitude on the SUES-200 benchmark for generalization-only models and our SFT framework. The top panel reports Drone→Satellite retrieval, while the bottom panel shows Satellite→Drone retrieval. In both directions, our method consistently achieves the highest R@1 across all altitudes and maintains a clear margin over all generalization baselines.

index such as FAISS on ℓ_2 -normalized descriptors so that inner products coincide with cosine similarities.

E Altitude-wise Analysis on SUES-200

Figures 8 and 9 further summarize the impact of drone flight altitude on retrieval performance in terms of R@1 and AP. Overall, all methods benefit from higher altitudes, since the drone viewpoint becomes more similar to the nadir-looking satellite imagery and the cross-view gap is reduced. However, the rate of improvement and the final performance plateau differ significantly across methods.

On the Drone→Satellite side, our method maintains a large and roughly monotonic improvement over generalization-only baselines. At 150 m we already exceed DINOv3 and AnyLoc by more than 40 points in R@1, and the gap further widens at 300 m, where our R@1 and AP are both above 90% while the strongest baseline remains below 60%. This suggests that the proposed 3DGS-based pseudo-orthophotos and drone-only Fisher aggregation are particularly effective at exploiting the reduced viewpoint gap at higher altitudes, whereas generalization-only baselines only partially benefit from the more nadir-like drone views.

A similar pattern is observed for Satellite→Drone retrieval, where absolute numbers are generally higher but the relative trends remain consistent. Our curves stay above those of all comparison methods at every altitude, and the margin over DINOv3 and AnyLoc is especially pronounced at medium-to-high altitudes (250–300 m).

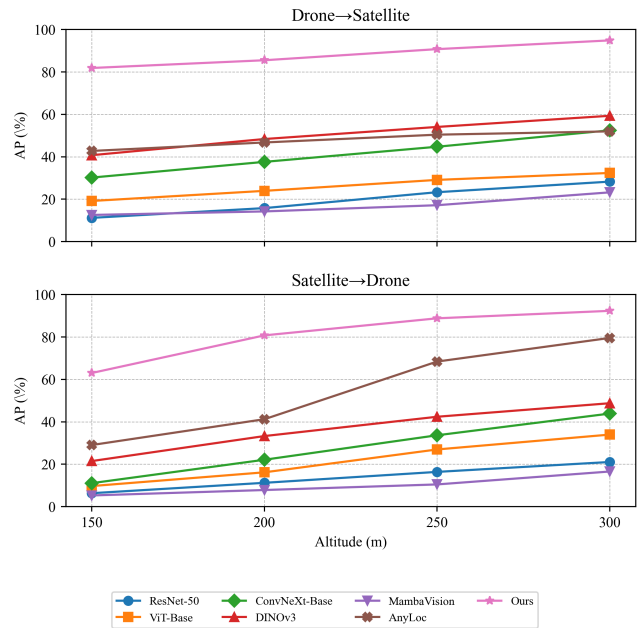


Figure 9: AP as a function of drone flight altitude on the SUES-200 benchmark for the same set of generalization-only models and our SFT framework. The overall trends are consistent with Fig. 8: our method provides substantial and stable gains in AP at all altitudes and in both retrieval directions, indicating improvements over the entire ranking rather than only at top-1.

Importantly, the AP curves in Fig. 9 exhibit the same trends as R@1, confirming that our gains are not limited to top-1 matches but translate into consistently better rankings over the entire gallery list. Taken together, these results suggest that the proposed satellite-free training pipeline is not only competitive in terms of final accuracy but also robust to changes in drone flight altitude, which is crucial for practical deployment in real-world drone missions.